

Frozen by heating: temperature controlled dynamic states in droplet microswimmers

Prashanth Ramesh ^{1,2} Yibo Chen ² Petra Räder,³ Svenja Morsbach ³ Maziyar Jalaal ⁴ and Corinna C. Maass ^{1,2,*}

¹Max Planck Institute for Dynamics and Self-Organization, Am Faßberg 17, 37077 Göttingen, Germany

²Physics of Fluids Group, Max Planck Center for Complex Fluid Dynamics and J. M. Burgers Center for Fluid Dynamics, University of Twente, PO Box 217, 7500AE Enschede, Netherlands

³Max Planck Institute for Polymer Research, Ackermannweg 10, 55128 Mainz, Germany

⁴University of Amsterdam, Science Park 904, 1098 XH Amsterdam, Netherlands

(Dated: August 16, 2024)

Self-propelling active matter relies on the conversion of energy from the undirected, nanoscopic scale to directed, macroscopic motion. One of the challenges in the design of synthetic active matter lies in the control of dynamic states, or motility gaits. Here, we present an experimental system of self-propelling droplets with thermally controllable and reversible dynamic states, from unsteady over meandering to persistent to arrested motion. These states are known to depend on the Péclet number of the molecular process powering the motion, which we can now tune by using a temperature sensitive mixture of surfactants as propulsion fuel. We quantify the droplet dynamics by analysing flow and chemical fields for the individual states, comparing them to canonical models for autophoretic particles. In the context of these models, we experimentally observe, in situ, the fundamental first broken symmetry that translates an isotropic, immotile base state to self-propelled motility.

I. INTRODUCTION

Active matter is defined by the nonlinear conversion of free energy on the molecular scale into macroscopic dynamics [1]: these nonlinear dynamics pose a challenge to the control of active agents, as small changes in system parameters can crucially tip the system over into a new dynamic equilibrium, for example from metastable inactivity to a state of directed motility.

More so, like a sorcerer’s apprentice [2] we find that stopping this motion is not a trivial task; after all, one is required to deplete an energy reservoir or reverse a dynamic instability [3].

This kind of control is important in the design and study of artificial and biological microswimmers, their theoretical modeling, experimental realization, and, ultimately, to provide design principles and dynamic control for technological application [4, 5].

Autophoretic particles [6–9] and, particularly, their experimental counterpart, active droplets [10–19], are popular active matter models driven by purely physicochemical mechanisms. Generally, their dynamics are characterized by a dimensionless Péclet number Pe , quantifying the ratio of advective and diffusive transport of chemical fuel [20]. With increasing Pe , autophoretic particles first transition from *passive* isotropic chemical conversion to *active* self-propulsion, and further from persistent to unsteady motion via a sequence of broken symmetries and interfacial flow modes of increasing complexity [18, 20–25].

Recent studies have investigated the control of speed and dynamic states of such microswimmers in response

to externally applied stimuli such as temperature [26, 27] or illumination [28–35].

On heating, physical intuition might suggest that motion should accelerate and destabilize, either by the increase of translational and rotational diffusion with decreasing viscosity, or by increased activity from the molecular thermodynamics driving the motion. However, the nonlinear dynamics of self-organized activity can drive counter-intuitive effects, as we have previously found for active droplets which destabilize with increasing viscosity due to an increase in Pe [24].

In this study, we explore another counter-intuitive response, this time to increasing temperature. We study active droplets using a temperature sensitive combination of co-surfactants in aqueous solution as a fuel medium. With increasing ambient temperature we find a transition between distinct dynamic states from unsteady to oscillatory to steady, straight swimming to eventual arrest, which is reversible and cyclic with temperature. Notably, by this method we are able to drive Pe across the critical activity threshold: we experimentally observe, live and in situ, the fundamental first symmetry breaking of the inactive isotropic base state into directed self-propulsion, analysing both chemical and hydrodynamic fields. This observation requires an undisturbed, unchanged ambient fuel medium, which we engineer by exploiting temperature dependent surfactant-polymer interactions [36] that were previously not considered in active droplets - opening new design possibilities to control the motion of micro-droplets as active agents in smart materials driven by purely physicochemical mechanisms [37].

* corinna.maass@ds.mpg.de

II. EXPERIMENTAL METHODS

A. Self-propelling droplets in co-surfactant solutions

Our experimental system consists of oil droplets (CB15) immersed in an aqueous solution of the ionic surfactant tetradecyltrimethylammonium bromide (TTAB) at 9-15 wt% (267–445 mM) and the triblock copolymer Pluronic F127 (PF127) at 4 wt%, or 3 mM.

CB15 droplets self-propel reliably in supramicellar solutions of pure TTAB above 5 wt% [24, 39]. Briefly put, the swimming is due to oil diffusing from the droplet into TTAB micelles [17, 19, 22], which removes surfactant from the droplet posterior, while the anterior is replenished by the advection of fresh surfactant (Fig. 1b). The key point here is that the empty micelles at the anterior are less thermodynamically stable than the oil-filled ones at the posterior [22, 40]: in consequence the critical micelle concentration is higher in front of a moving droplet. The resulting self-enhancing surface tension gradient drives the droplet forward until it is dissolved. Typically, a CB15 droplet of diameter 50 μm will swim in 5 wt% TTAB for 1-2 hours. Based on this mechanism, one can define a Pe of droplet motion that increases with viscosity, droplet radius and surfactant concentration, i.e. chemical activity [18, 22, 24, 25, 41]. In a surfactant solution where all micelles are oil-saturated, droplets would not propel, and they are repelled by gradients in filled and attracted by gradients in empty micelles [39]. We may in this sense regard empty TTAB micelles as fresh, and oil-filled ones as spent fuel.

PF127 is a nonionic triblock copolymer surfactant that in a pure aqueous solution forms micelles with a hydrophobic core of propylene oxide (PPO) and an outer shell of hydrated ethylene oxide (PEO) [42–47] above the critical micelle temperature, $\text{CMT} \approx 21^\circ\text{C}$ at 4 wt% PF127 [44]. In the presence of ionic co-surfactants like TTAB, which bind strongly with PF127, mixed TTAB/PF127 aggregates form (Fig. 1a, Appendix C, Figs. C.1, C.2 and C.3), with excess TTAB forming single-species micelles [36, 38, 48, 49]. It has been found [49] that the TTAB binding capacity of PF127 is amplified with increasing temperature, due to an increasing dehydration of the PPO blocks (hydrophobic effect [42, 50]).

Under our experimental conditions, we expect a significant coverage of TTAB at the interface (Appendix Fig. D.1). Furthermore, CB15 droplets are completely immotile and hardly solubilize in pure PF127 solutions (Appendix Fig. D.2), while in a mixed TTAB/PF127 medium self-propelling at speeds $\approx 20 \mu\text{m/s}$, comparable to experiments in pure TTAB solutions (cf. [24, 39] and Appendix Fig. E.1). We therefore regard TTAB as the primary surfactant mediating the solubilization and the interfacial gradients driving the droplet motion. This activity is controlled by PF127 binding and releasing TTAB micelles in the bulk medium (Fig. 1a,b). Thus, the Péclet

number Pe of droplet activity *decreases* with *increasing* temperature, as an increasing fraction of TTAB is bound in mixed micelles.

According to literature on the composition of PF127/TTAB aggregates [48, 49, 51], the amount of bound TTAB in our swimming medium should exceed 1 wt% and further increase with temperature, which is on the order of the amounts required (< 5 wt%) to suppress droplet motility [19, 24], as observed in the experiments we show below (see also Appendix Fig. A.1). We further note that the swimming medium is Newtonian, with only weakly temperature dependent viscosity (Appendix Fig. G.1).

III. RESULTS

A. Swimming dynamics controlled by temperature and fuel concentration

We begin with an overview of the general swimming dynamics taken from wide-field video microscopy under changing the ambient temperature, and for a range of TTAB concentrations. The setup contains a quasi-2D microfluidic cell on a temperature controlled stage (Fig. 1c). Fig. 2a (Movie S1) plots a trajectory colour-coded once by speed and once by temperature, recorded at a set heating/cooling rate of 1 K/min, using a swimming medium containing 10 wt% TTAB.

We start at $T \approx 15^\circ\text{C} < \text{CMT}$. Below $T_{\text{straight}} = 22^\circ\text{C}$, the droplet meanders, i.e. periodically reorients. Above, the motion is straight, gradually slows down and eventually stops at $T_{\text{stop}} \approx 27^\circ\text{C}$. During a subsequent cooling ramp, the droplet remains immotile down to a significantly lower temperature $T_{\text{start}} \approx 17^\circ\text{C}$, where it abruptly starts to meander again.

As well as by temperature, the swimming dynamics are also susceptible to the TTAB concentration. Previous studies on reference systems using a single surfactant species found a transition from straight to reorienting to unsteady swimming [22]. Here, in response to an increase in surfactant concentration, Pe increases, and destabilizing higher order modes in the interfacial flow and chemical fields emerge. Similar mode changes have been found if Pe is increased via the droplet size or the viscosity of the swimming medium [24, 25, 41]. These effects are consistent with analytical models for isotropic autophoretic particles [14, 20, 25, 52, 53], in the weakly nonlinear limit, and numerical studies [54, 55], in the chaotic limit.

At low temperatures, the presence of a co-surfactant does not change these dynamics, as we find a transition from meandering to unsteady motion (Fig. 2d, Movie S2) with increasing TTAB concentration. We have summarized these swimming dynamics in a map spanned by temperature and surfactant concentration in Fig. 2b. With increasing temperature, we observe a universal transition via straight swimming to eventual arrest. We posit that the temperature dependent TTAB depletion

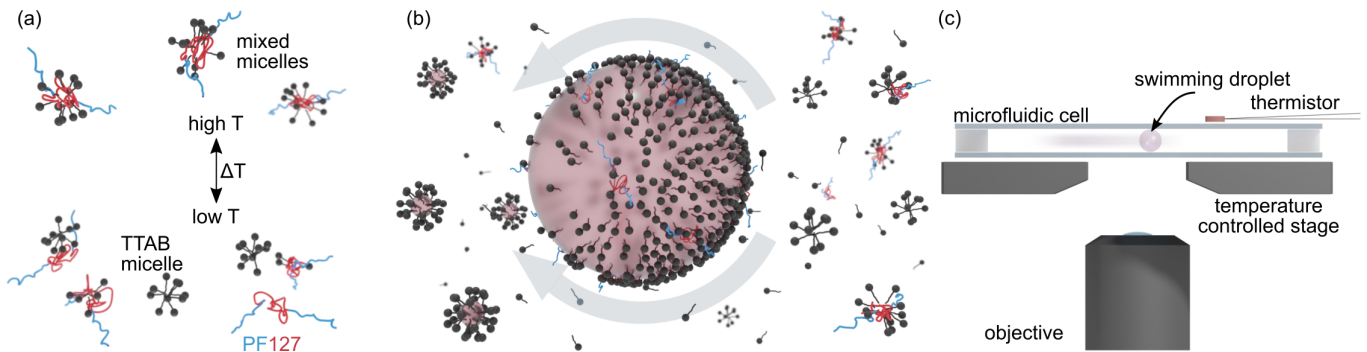


FIG. 1. **Schematics of the experimental setup and droplet propulsion mechanism.** (a) With increasing/decreasing temperature, there is an increased/decreased affinity for TTAB to form mixed micelles with PF127. Simplified aggregation schematic [38]. (b) Droplet propulsion during solubilisation: an inhomogeneous distribution of empty TTAB micelles causes a self-sustaining Marangoni gradient at the oil-water interface. (c) Setup: The droplet (diameter $d = (50 \pm 5) \mu\text{m}$) swims in a quasi-2D ($13 \text{ mm} \times 8 \text{ mm} \times 50 \mu\text{m}$) cell on a temperature controlled microscope stage. All schematics are not to scale.

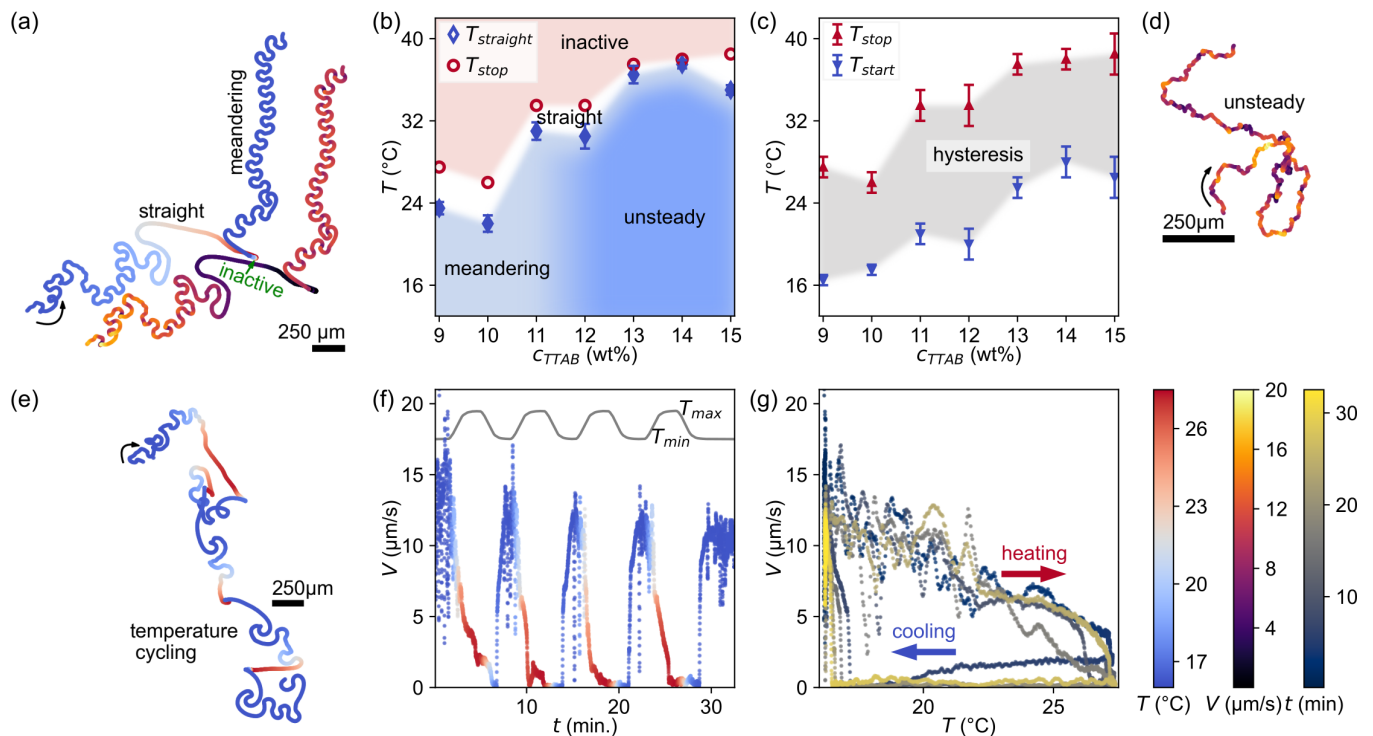


FIG. 2. **Swimming dynamics controlled reversibly via temperature and fuel concentration** (a) Droplet trajectory transitioning from meandering to straight swimming to arrest during a heating and subsequent cooling ramp with a set rate of 1 K/min in a mixed surfactant swimming medium, color coded by droplet speed and recorded temperature. See also Movie S1. Color map and scale bars ($250 \mu\text{m}$) apply to all figures in the paper, and concentrations for PF127 and TTAB are always 4 wt\% and 10 wt\% , respectively, unless stated otherwise. (b) Map of the swimming dynamics depending on temperature and surfactant concentration. (c) Hysteresis between droplet stop and start transition temperatures. Error bars also apply to T_{stop} in (b); experiments done in triplicate with 5–10 droplets each. (d) Example of unsteady motion at 15 wt\% TTAB and $21 \text{ }^\circ\text{C}$ (see also Movie S2). (e) Droplet trajectory during multiple heating/cooling cycles set at 10 K/min and 10 wt\% TTAB. See also Movie S3. (f) Corresponding droplet speed vs. time, with inset plot of the recorded temperature ramps. (g) Droplet speed vs. recorded temperature showing a hysteresis in the re-onset of motion during cooling: the arrest during cooling is extended, with a sudden recovery of the initial speed at $T \approx 17 \text{ }^\circ\text{C}$.

lowers Pe below the critical thresholds of higher order interfacial modes, down to $n = 1$ for straight swimming and finally $n = 0$, below the fundamental advection-diffusion instability. We do not provide a quantitative estimate of Pe following [24], as we cannot quantify the temperature dependence of the underlying physical chemistry parameters. Fig. 2b also shows a general trend of the transition temperatures to increase with TTAB concentration: for the droplet to arrest, more TTAB needs to be removed from the swimming medium. We found the stop/start hysteresis for all TTAB concentrations in use (Fig. 2c).

These state transitions are well reversible with temperature, up to some slowdown attributable to droplet shrinkage. The experiment shown in Fig. 2e-g and Movie S3 was recorded at a faster rate of 10 K/min to permit multiple heating and cooling cycles, with dynamics similar to the system cooled at slower rates. Fig. 2e and f show the droplet trajectory color coded by temperature and a corresponding plot of speed over time. The initial motion is recovered after each heating and cooling cycle, apart from a very gradual decrease in maximum speed which we may attribute to droplet shrinkage. We have further analyzed speed versus temperature in Fig. 2g, and found a hysteresis cycle with a delayed re-onset of motion reproducible over multiple heating/cooling ramps. The sample in Movie S3 contained three larger droplets ($d \approx 60 \mu\text{m}$): Pe should increase with the droplet radius, and, correspondingly, these droplets switch from reorienting to straight motion at later times and therefore higher temperatures.

B. Chemical and flow fields

We continue with a discussion of the chemical dynamics during the droplet arrest, to motivate the hysteresis in the re-onset of motion; and of the corresponding flow field to investigate the interfacial mode evolution.

The self-generated field of spent fuel in the local environment affects the droplet motility, both via chemorepulsive gradients [22, 24] and via accumulation of filled micelles, which suppresses the interfacial activity [56]. We visualise this field by doping the droplet with the fluorescent dye Nile Red [57], which co-moves with the oil phase into the filled micelles, and extract the fluorescence intensity I from videomicroscopy data (Movie S4). In Fig. 3, we analyze these chemical dynamics for one droplet during a heating and cooling cycle, showing a speed-coded trajectory (a), a kymograph of I around the droplet perimeter, θ vs. time and recorded temperature (b), and micrographs at the times marked I–IV (c).

During heating, the droplet transitions from unsteady to straight swimming to immotility (Fig. 3a). We note that this particular experiment featured some global drift causing translation even in the immotile state (see Movie S4). In the kymograph (Fig. 3b), at $T < 26^\circ\text{C}$, the band corresponding to the chemical trail translates in the angular space due to the reorientation of the droplet (I). At

$T \approx 26^\circ\text{C}$, the droplet slows down and comes to a halt. As the system is cooled down to $T \approx 21^\circ\text{C}$, the inactive droplet still solubilises isotropically, and oil-filled micelles accumulate around the perimeter θ . Correspondingly, the band in the kymograph widens over the entire angular space (II). The accumulated filled micelles block empty micelles from reaching the interface [53, 56], such that in the presence of oil-filled micelles even more mixed micelles need to disintegrate to restart activity. Thus, the motility transition temperature is lowered, here to $T_{\text{start}} = 16.8^\circ\text{C}$, where the droplet escapes the oil-filled micelle cloud (III) and swims away (IV).

Before discussing the flow fields, we note two more consequences of oil saturation. First, the hysteresis in Fig. 2c is reduced by several degrees if the system is not heated to full droplet arrest, but it is never entirely suppressed (Appendix Fig. Fig. F.1). This can be understood as follows: during the late stage of the heating ramp, the droplet is already dispersing oil into its local environment by recirculation, starting from the posterior - an effect we have also found in self-throttling pumping droplets in [56]. During heating, the droplets will come to a stop even before the interfacial activity has fully ceded (see the discussion of Fig. 4b below), and self-propulsion would always need to restart from inside an oil-rich region as shown in Fig. 3c-II.

Second, the regime of straight swimming appears to be highly localized on cooling (Movies S1 and S6): the droplet switches after a few seconds after a meandering motion (Movie S1). We argue here that outside the strongly localized cloud of spent fuel (see Movie S4 and Fig. 3c), more empty TTAB micelles have been released, such that the droplet experiences a higher Pe once it escapes its self-generated local trap. We note that during this escape there is a radial gradient from filled to empty micelles, which would also locally rectify the droplet motion.

To analyze the mode evolution causing arrest and sudden onset of motion during heating and cooling (Movie S5), we added tracer colloids to the oil phase, performed high resolution bright field videomicroscopy and analyzed the internal flow field $\mathbf{u}(x, y)$ by particle image velocimetry (PIV) at a series of equilibrated set temperatures. Fig. 4b shows the evolution of \mathbf{u} with increasing temperature. At $T = 16^\circ\text{C}$, we see a mixed dipolar and quadrupolar flow field (modes $n = 1, 2$) corresponding to the meandering trajectory in Fig. 2a [24, 25]. At even higher temperature, $T = 21^\circ\text{C}$, the droplet swims straight, Pe decreases and the flow field is purely dipolar ($n = 1$). As the droplet begins to slow down, an inactive region spreads from the droplet posterior ($T = 24^\circ\text{C}$). Finally ($T = 27^\circ\text{C}$), just before the droplet stops ($n = 0$), only a small region at the droplet anterior is active [56]. As shown in Fig. 3III, the local environment isotropically saturates with spent fuel while the droplet is immotile.

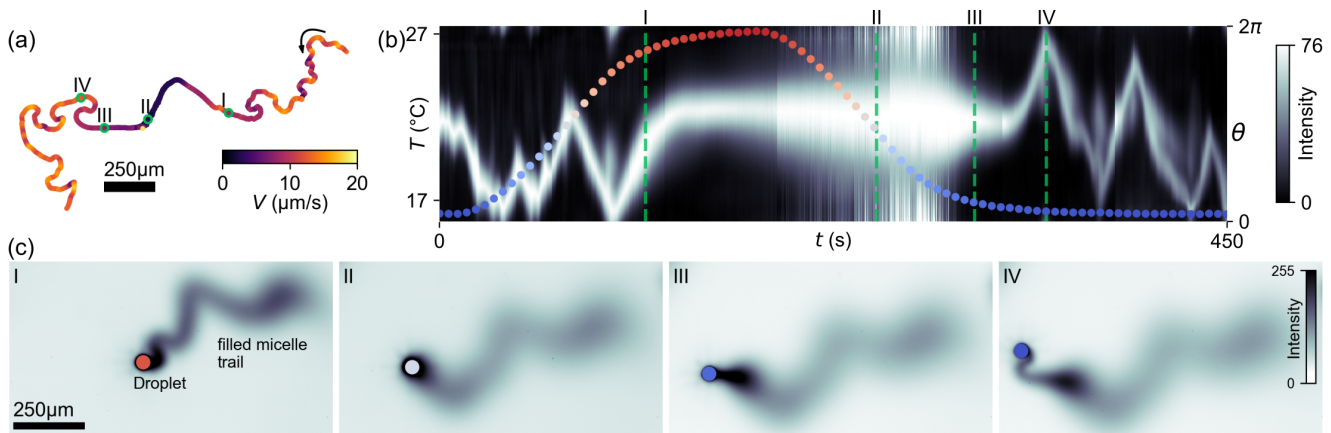


FIG. 3. **The hysteresis in the re-onset of droplet motion is caused by spent fuel aggregation.** (a) Droplet trajectory during heating and subsequent cooling ramp color coded by speed. (b) Kymograph showing the evolution of chemical concentration field around the droplet interface and the recorded temperature (colored symbols). (c) Snapshots of droplet chemical trails at different temperatures as marked by I-IV in (a) and (b). See also Movie S4. 250 μm scale bars and colour maps as defined in Fig. 2.

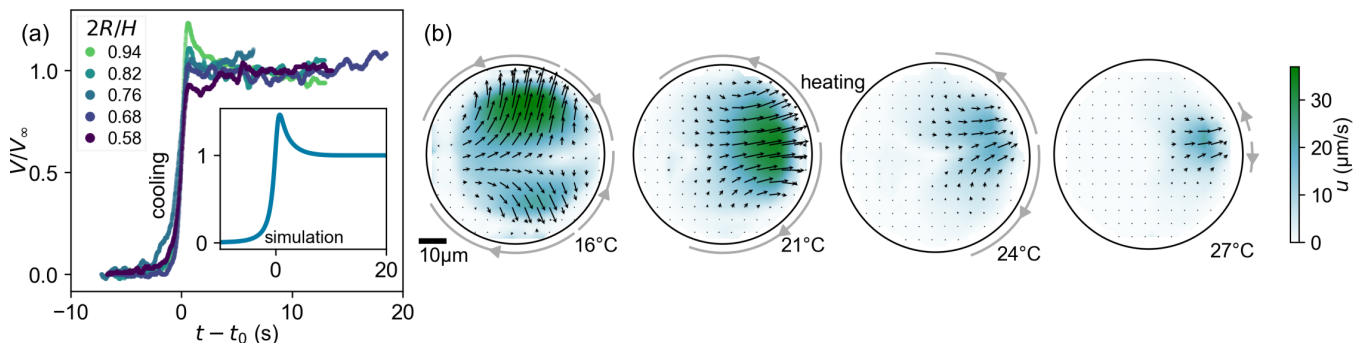


FIG. 4. **Observation of the transition between passive dissolution and active propulsion.** (a) Onset of motion during re-cooling, speed (normalized to steady state V_∞) vs. time for multiple runs with t_{onset} corresponding to $(dV/dt)_{\text{max}}$. The initial overshoot increases with confinement $2R/H$. Inset: simulation for an isotropic autophoretic particle under comparable conditions ($H = 2.2R$ confinement, $Pe = 8$), redimensionalised (Appendix J and Movie S6). (b) Internal flow field with increasing temperature, starting at a mixed dipolar/quadrupolar mode (meandering), over a purely dipolar mode (straight) that recedes to the anterior (slowdown). Vectors and color map inside the droplet indicate the velocity field $\mathbf{u}(x, y)$; arrows around the perimeter mark the active regions on the droplet interface. Scale bar 10 μm.

C. Simulations

The gradual increase of Pe during cooling now allows us to directly observe the fundamental first transition from the immotile base state to self-propelled motion [14, 20]. This can be motivated theoretically using hydrodynamic advection-diffusion models, canonically derived in [20] as follows:

A spherical particle of radius R is immersed in a fluid medium containing a chemical fuel at concentration c . At negligible Reynolds numbers, the flow is governed by the Stokes equations, $\mu \nabla^2 \mathbf{u} = \nabla p$, $\nabla \cdot \mathbf{u} = 0$. The chemical field is coupled by an advection-diffusion equation,

$$|Pe| \left(\frac{\partial c}{\partial t} + \mathbf{u} \cdot \nabla c \right) = \nabla^2 c, \quad Pe \equiv \frac{\mathcal{A}MR}{D^2}, \quad (1)$$

and by the particle consuming fuel at its boundary, $\partial_t c(R) = -\mathcal{A}$. The Péclet number is set by the activity \mathcal{A} , mobility \mathcal{M} and diffusivity D of the chemical species and the particle radius R . Using a decomposition into squirmer modes and a linear stability analysis around the isotropic base state (mode $n = 0$), the authors of [20] find a transition to the propulsive dipolar state ($n = 1$) above a threshold value of $Pe = 4$.

The mixed surfactant approach allows us to observe the growth of the dipolar mode in situ and analyzing it in the context of the canonical model. We performed a simulation of the interfacial instability, following [20, 58],

here solving for the full 3D problem and adapted to our cell geometry (see Appendix J), and compared it to the experimental droplet speed V at the onset of motion, with good agreement between re-dimensionalised numerical and experimental results (Fig. 4a, Movie S6). For one, the timescales for the onset of motion, of $\mathcal{O}(1\text{ s})$, and the evolution of the steady state at V_∞ , of $\mathcal{O}(5\text{ s})$, are similar. Second, there is a characteristic overshoot in V/V_∞ shortly after the onset of motion, common to various numerical approaches [59, 60], and already noted as ‘surprising’ in [20]. This initial push could be provided by the diffusive cloud of consumed or depleted fuel around the droplet (see eg. Fig. 3c-II), which causes a radial chemorepulsive gradient. Such gradients would be enhanced by confinement [58, 61]: simulations have found the overshoot to increase with confinement [58], and we find a similar tendency in our experimental data (Fig. 4(a)).

IV. CONCLUSIONS

Tuning the dynamics of self-propelling droplets by temperature-driven surfactant interactions provides a promising framework to regulate micelle-mediated [62, 63] active droplet dynamics: we can now control self-propulsion from an unsteady or meandering state over quasi-ballistic propulsion to full arrest without needing to change the chemistry of the system. The gait control is encoded in the swimming medium and does not require complex micro-engineered swimmer design. Since the hydrophobic effect underlying the temperature dependent complex formation is entropy driven and similar aggregation effects are established for numerous surfactant-polymer combinations [36, 38, 48, 49, 64], this control method likely applies to active droplet models driven by micellar solubilisation in general, and could be tested in further studies, e.g. for SDS surfactant or DEP oil [22, 65]. The transitions are almost fully reversible, excepting a slight reduction in peak speed that can be attributed to droplet shrinkage.

Our hypothesis – fuel binding by thermosensitive polymer cosurfactants – does not account for the dynamics of adsorbed polymer at the interface, which might also be temperature dependent. However, we argue that these effects are, if present, secondary to the binding and release of TTAB in the swimming medium: generally, the desorption kinetics of large polymers are assumed to be exceedingly slow [50]. Thus, if these kinetics were the main drivers of thermoresponsive mode switching, it would not be consistent with our observations of cyclic reversibility and the fast response to changed external conditions, i.e. the instantaneous onset of motion in Fig. 4a and particularly the fast, local adaptation to the fuel-rich medium outside the saturation area.

Our experiments fit into the framework of the canonical theory for autophoretic particles, where the observed dynamic regimes correspond to interfacial modes becom-

ing unstable with increasing or decreasing Péclet number.

While such higher order modes have been documented individually, the fundamental spontaneous transition from an isotropic zero order base state to a first order propulsion state is hard to observe experimentally, as the setup of the experiment usually provides sufficient disturbances to instantaneously set off droplet motion. By a non-invasive temperature driven crossing of the critical Pe threshold, this is now experimentally observable in both chemical and flow signatures.

Acknowledgements

We thank Dr. Babak Vajdi Hokmabad, Dr. Kevin Zhong and Dr. Stefan Karpitschka for invaluable advice and discussions, Dr. Stephan Weiss for providing the thermistor and Dr. Kristian Hantke for experimental support.

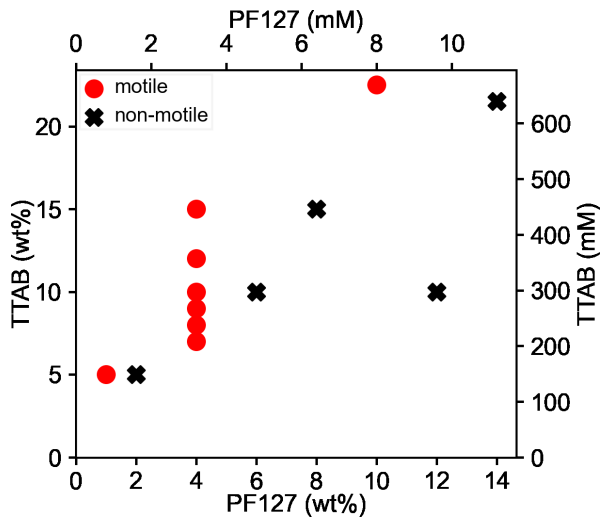


FIG. A.1. Motility chart for $50\ \mu\text{m}$ droplets in media of various surfactant composition, taken at room temperature.

Appendix A: Materials and characterization

We obtained CB15 (Synthon Chemicals), TTAB and PF127 (Sigma-Aldrich) and used them as-is. To study the influence of mixed micelles on active droplet motility around room temperature, we varied the TTAB concentration between 9–15 wt%. We note that a low concentration of PF127 requires heating the system to high temperatures to deplete TTAB, causing evaporation issues, while at a higher concentration of PF127 droplets would only be active at low temperatures. This strongly limited the experimentally accessible parameter space for PF127, and we opted to keep the concentration fixed at 4 wt%. An overview of the media compositions for which we observed swimming at room temperature (22°C) is shown in Fig. A.1. Increasing the amount of PF127 suppresses motility, while an excess of TTAB promotes it. The typical molarity ratios for motility are of the order of 1:100.

Appendix B: Microfluidic experiments

We mass produced CB15 droplets in microfluidic flow focusing devices [24] at a size of $(50 \pm 5)\ \mu\text{m}$. We fabricated the experimental reservoir, a Hele-Shaw geometry, by spin coating a $50\ \mu\text{m}$ layer of SU-8 photoresist on glass, and creating a rectangular void space of area $(13 \times 8)\ \text{mm}^2$ by UV photolithography. For experiments, we filled it with a dilute droplet emulsion and sealed it with a glass cover slip. The Rayleigh number, estimated for an aqueous medium, a typical lengthscale of $50\ \mu\text{m}$ and $\Delta T = 10\ \text{K}$, is $Ra \approx 10^{-2}$, ruling out thermal convection effects.

We recorded the motion of active droplets on a bright-field microscope (Olympus IX-81) with a temperature

Plot	Settings
Fig. 2a	1 K/min
Fig. 2e-g	10 K/min
Fig. 2b,c	5 K/min
Fig. 3	5 K/min
Fig. 4	stepwise heating, ≈ 3 min equilibration before data acquisition

TABLE B.1. Summary of heating rates/protocols for the data underlying the figures in the manuscript.

controlled stage (Linkam PE100) which allowed for both heating and cooling protocols. We set the reservoir temperature at the desired initial value for a period of 5 min, after which we started measurements.

We performed temperature ramp experiments with a set heating/cooling rate of 1 K/min, 5 K/min or 10 K/min. As shown in Fig. 2 (c), the system did not equilibrate instantaneously. We therefore directly measured the sample temperature using a thermistor taped to the coverslip sealing the microfluidic reservoir (Fig. 1). Movie frames were recorded at 4 frames per second (fps) using a Canon digital camera (EOS 600d) with a digital resolution of $1920 \times 1080\ \text{px}$.

We chose heating/cooling rates based on the experimental parameters and the required degree of quantitation. The minimum rate was limited by droplet shrinkage over time. Slower heating rates were feasible for single-cycle experiments, low TTAB concentrations and temperatures. Table B.1 summarises the protocols for the data underlying Fig. 2-4 and the corresponding supporting videos. For the best determination of T_{start} , T_{straight} , and T_{stop} , the rate was kept as low as possible, we ensured via the recorded droplet sizes that the polydispersity was low, $(50 \pm 5)\ \mu\text{m}$, and used small number densities ($< 0.1\ \text{mm}^{-2}$) to exclude mutual trail interactions.

To estimate whether the quasi 2D confinement affects the observed dynamics, we have also recorded the temperature-dependent droplet motion in reservoirs with a larger height of $310\ \mu\text{m}$ and $2\ \text{mm}$, using a swimming medium with 10 wt% TTAB and 4 wt% PF127. We found similar dynamic states and, within the experimental error (see Fig. 2b), the same transition temperatures ($T_{\text{straight}} \approx 23^\circ\text{C}$, $T_{\text{stop}} \approx 27^\circ\text{C}$) as in the case of the quasi-2D geometry, $h = 50\ \mu\text{m}$ (Fig. 2b).

Appendix C: Investigation of TTAB/PF127 micelle formation

To investigate the formation of individual and mixed micelles in our particular swimming medium, we recorded dynamic light scattering and calorimetry data on solutions of pure and mixed surfactants. The nature of these complexes is according to existing literature highly dependent on concentrations and temperature, however, at the relative concentrations exceeding 1:100 in our system, PF127 micelles are presumably fully broken down

for the entire temperature range under investigation [49]. For this reason, we do not expect the CMT of PF127 to be a characteristic quantity in the dynamics of our system.

1. DLS measurements

We performed dynamic light scattering (DLS) measurements for the co-surfactant mixtures used in our experiments on a Malvern Zetasizer Ultra Red. We placed a 1 mL sample in a polystyrene cuvette and recorded the backscattering intensity at 173° between 15°C and 30°C . At each temperature, the sample was allowed to equilibrate for 120 s, and all measurements were carried out in triplicate. We have plotted the size distributions for selected temperatures in Fig. C.1 and summarized the temperature dependent behaviour for all samples via the Z average hydrodynamic diameter, i.e. the “intensity weighted mean hydrodynamic size of the ensemble collection of particles” (Malvern) in Fig. C.2. For 4 wt% PF127, there is a significant increase in diameter above 23°C , corresponding to the formation of PF127 micelles (we note that this appears somewhat higher than the CMT $\approx 21^\circ\text{C}$ literature value [42, 44]). This increase is suppressed in the presence of TTAB, consistent with the formation of PF127/TTAB complexes seen in literature [38, 48, 49, 64]. We note that, from the Z average, the hydrodynamic diameter of these complexes is somewhat smaller than that of a PF127 monomer, which is in line with existing studies [64]. Further, these complexes appear to be close in size to pure TTAB micelles in a size range $< 5\text{ nm}$ near the lower DLS resolution limit, such that the two species probably cannot be resolved in Fig. C.1.

2. Differential scanning calorimetry

We investigated the temperature dependent PF127 micellization using differential scanning calorimetry (DSC). For the measurements, we prepared three sample types: (1) PF127 in 4 wt% water, (2) PF127 4 wt% + TTAB 1 wt% in water and (3) PF127 4 wt% + TTAB 10 wt% in water. Solutions were directly transferred into DSC sample aluminium pans (volume $100\ \mu\text{L}$, Mettler-Toledo GmbH, Gießen, Germany). DSC pans were covered with aluminum lids. DSC measurements were performed on a DSC 823 instrument (Mettler-Toledo GmbH, Gießen, Germany). Heating-cooling cycles were recorded at a heating/cooling rate of 5 K/min between 0 and 80°C . The measurements were performed under a nitrogen atmosphere with a flow of 30 mL/min . Heating curves were normalized to the sample mass. The endothermic dip in the curve for pure PF127 is consistent with the onset of micellization from the DLS results, and is similarly suppressed under the addition of TTAB.

Appendix D: Cosurfactants on oil-water droplet interfaces

We conducted further experiments to confirm, under our experimental conditions, (A) that TTAB is the dominant surfactant at the oil-water interface and (B) that the aqueous solubilization of CB15 is mainly TTAB mediated, as follows.

1. TTAB interfacial coverage based on nematic anchoring

In liquid crystal emulsions, the interfacial anchoring of the nematic director depends on the surfactant in use. Assuming comparable interfacial activity for both substances, we can infer the presence of TTAB at the oil-water interface from investigating the anchoring for CB15’s nematic isomer 5CB (at room temperature) under polarised microscopy [66, 67]. We show this in three micrographs in Fig. D.1: 5CB droplets (left) in 0.1 wt% TTAB show a cross-shaped interference pattern and a central point defect, consistent with homeotropic (surface normal) anchoring as known for TTAB. On the right, we show a droplet in 0.005 wt% TTAB and 4 wt% PF127, where we observed a bipolar defect pattern, with two opposing defects at the interface (one visible in the micrograph). This pattern is typical for planar anchoring, and we associate it with the large excess of PF127. In the middle image, for 1 wt% TTAB and 4 wt% PF127 (middle), there is only a single point defect, indicating a transition to TTAB mediated homeotropic anchoring already far below the 10 wt% TTAB used in the experiments on motile droplets.

2. Solubilization rate measurements

We measured the shrinking rate of a CB15 droplet for two non-motile cases under bright field microscopy at 63x magnification – 10 wt% TTAB + 12 wt% PF127 and 4 wt% PF127, both at 40°C – and in an ensemble average of motile droplets under typical experimental conditions, 10 wt% TTAB + 4 wt% PDF127 at 20°C under 4x magnification; droplet radii and fitted shrinking rates are shown in Fig. D.2. Dissolution is reduced by an order of magnitude without TTAB.

Given that (A) there appears to be a considerable fraction of TTAB at the interface and that (B) droplets neither significantly dissolve or move in pure PF127, we conclude that the droplet motion is primarily driven by TTAB gradients in the oil-water interface, by a mechanism similar to the one driven by micellar solubilization found in pure TTAB media [10, 17, 19]. We also note that the droplet speed is of a similar order of magnitude as the one in pure TTAB ($\approx 10\text{--}20\ \mu\text{m s}^{-1}$, Fig. E.1), such that additional adsorbed PF127 at the interface does not appear to impede the mechanism.

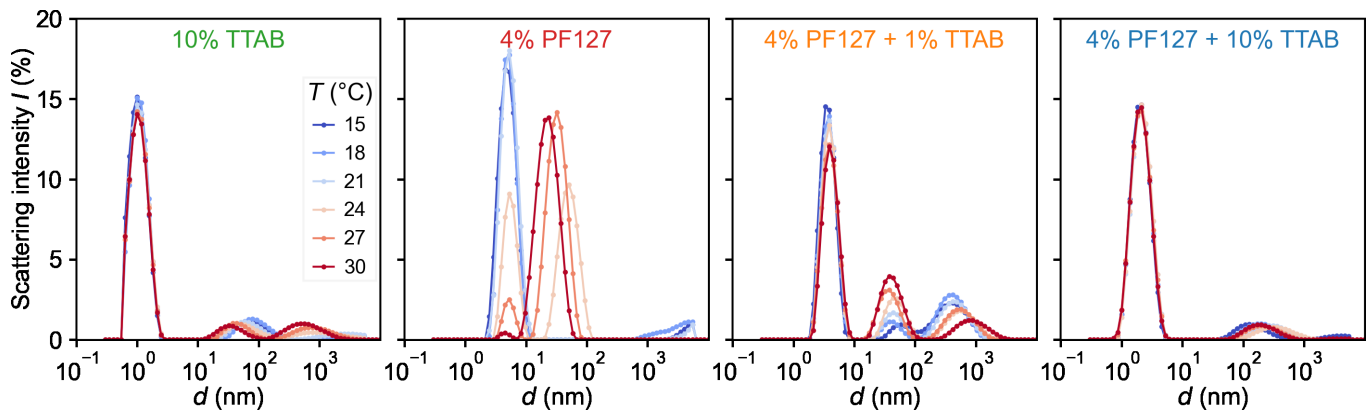


FIG. C.1. Dynamic light scattering (DLS) measurements showing the size distributions of four aqueous solutions of PF127 and TTAB with increasing temperature, from backscattering (detector angle 173°). Scattering intensity I vs. hydrodynamic diameter d . Averages over triplicate measurements.

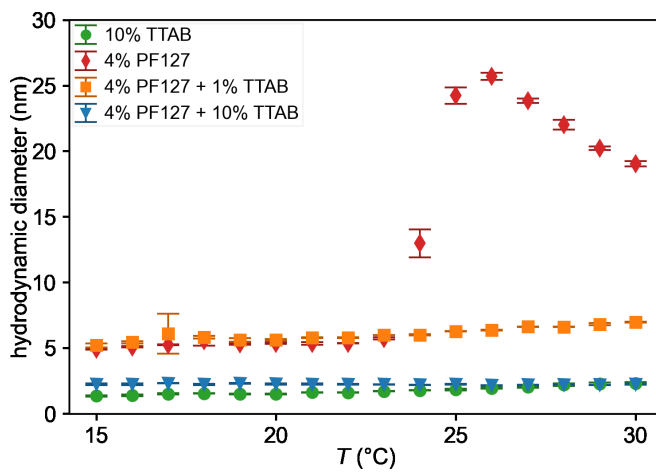


FIG. C.2. Intensity weighted Z-average values of the hydrodynamic diameter for each measurement as shown in the DLS series in Fig. C.1. The error bars use the standard deviation of the triplicate experimental runs.

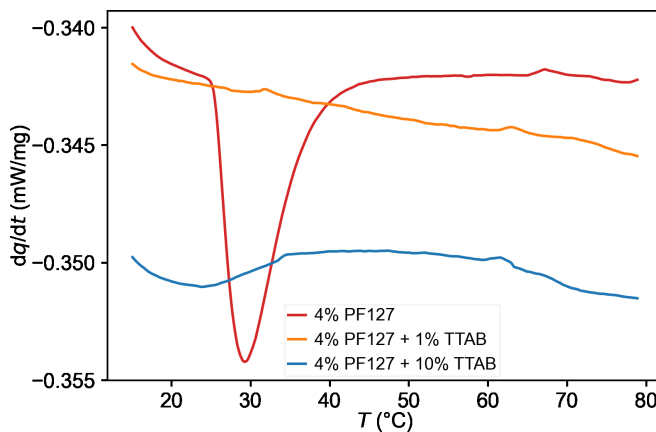


FIG. C.3. DSC heating curves of PF127 and TTAB solutions. Measurements were performed with a heat rate of 5 K/min and normalized to sample mass.

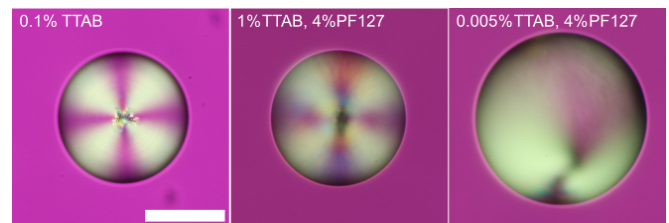


FIG. D.1. Polarized micrographs of 5CB droplets in cosurfactant mixtures: left, 0.1 wt% TTAB, shows homeotropic; right, 4 wt% PF127 and 0.005 wt% TTAB, planar anchoring; middle, 4 wt% PF127 and 1 wt% TTAB, primarily homeotropic. Scale bar $50\ \mu\text{m}$

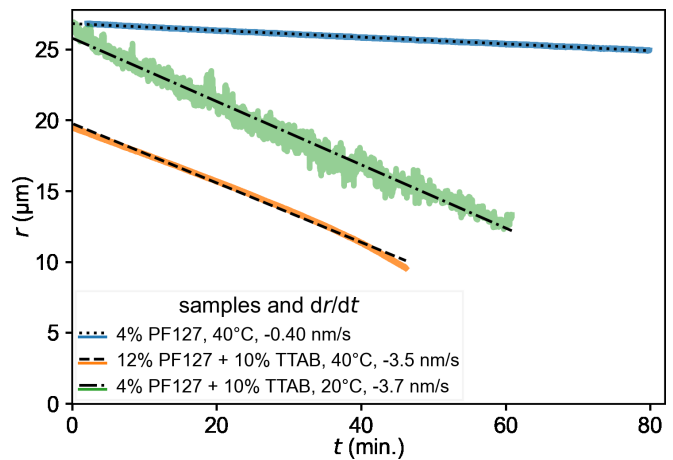


FIG. D.2. Decrease in CB15 droplet radius over time for non-motile droplets in 4wt% PF127 (blue) and 12wt% PF127 + 10wt% TTAB (orange) media at $T = 40^\circ\text{C}$ (one droplet each at 40x magnification), and for motile droplets in 10wt% TTAB + 4wt% PF127 at 20°C (green, low magnification ensemble average). Dotted lines: linear regression fits to determine the shrinking rates, -0.4 nm/s , -3.5 nm/s and -3.7 nm/s , respectively.

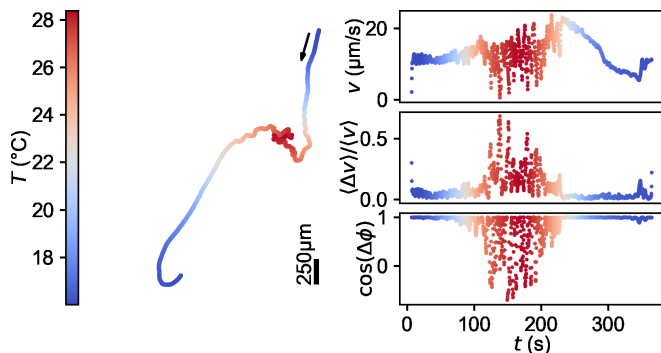


FIG. E.1. Temperature dependent droplet dynamics in a solution of pure TTAB at 10 wt%. (a) Droplet trajectory and (b) droplet speed v , and measures of fluctuations in speed, $\langle \Delta v \rangle / \langle v \rangle$, and orientation, $\cos(\Delta\phi)$, over time. With increasing temperature, the droplet motion accelerates and destabilises. Scale bar 250 μm .

Appendix E: Temperature dependent dynamics in pure TTAB solution

In Fig. E.1, we show a temperature-coded trajectory of a droplet studied under the same conditions as the experiments shown in the main manuscript, but in an aqueous solution of TTAB only at 10 wt%. Here, the motion destabilises with increasing temperature. We illustrate this by temperature-coded plots of three quantities: the speed (top), which increases, but also fluctuates strongly for high temperatures. Further, two simple correlation estimates, both taken over a running time window of $\tau = 2$ s: the standard deviation over average speed, $\langle \Delta v \rangle / \langle v \rangle$ as a measure of unsteadiness in speed, and the cosine of the angle between $\mathbf{v}(t)$ and $\mathbf{v}(t + \tau)$ via their inner product as a measure of rotational fluctuation. Both indicate strong decorrelation at elevated temperatures. We note that this behavior is strongly different from the one in PF127/TTAB mixtures, where speed and unsteadiness decrease with increasing temperature.

Appendix F: Reduced hysteresis during an incomplete heating ramp

We have found a reduction in hysteresis to about half the temperature difference when the droplet does not fully stop (i.e., during an incomplete heating ramp, where it slows down to $< 1 \mu\text{m/s}$). Fig. F.1 shows an example for 13 wt%, with the speed coded trajectory in (a), speed and temperature over time in (b) and in (c), for comparison, the same quantities for the trajectory plotted in Fig. 2a in the MS. Compared to the $T_{\text{start}}, T_{\text{stop}}$ values for $c_{\text{TTAB}} = 13 \text{ wt}\%$ in Fig. 2c, the hysteresis is reduced almost by half, the droplet doesn't stop entirely and the re-onset of motion is far more gradual than one starting from full arrest (see zoomed in inset in (c)).

Appendix G: Viscosity measurements

We measured the viscosity of our swimming media on an Anton-Paar MCR 502 rheometer using a cone-plate geometry with a gap width of 0.1 mm. Measurements were carried out at temperatures between 15 °C and 40 °C and shear rates between 0.1 s^{-1} and 100 s^{-1} (see Fig. G.1). We observe Newtonian rheology and an only weakly temperature dependent viscosity. Thus, while aqueous solutions of PF127 are known to gel at high temperatures, essentially forming a network of micelles, we are still below this non-Newtonian regime at the concentration and temperature range in use.

Appendix H: Flow and chemical field measurements

The internal flow field was determined by adding $1 \mu\text{m}$ diameter tracer Silica particles (Cospheric SiO2MS-1.8) to the oil phase and analysing high magnification videomicroscopy data by particle image velocimetry (PIV). We did not measure external flow fields, since adsorbed PF127 on colloidal tracer particles [68] may cause them to aggregate and impedes accurate PIV measurements.

We recorded videomicroscopy data under a 40x objective using a 4MP camera (FLIR Grasshopper 3, GS3-U3-41C6M-C) at 40 fps at different set temperatures.

To study the sudden onset of motion from an inactive state as the system was cooled, images were recorded at a higher frame rate of 80 fps. Droplet speed over time was calculated from the recorded trajectories.

To visualize the oil-filled micelle chemical trail behind the droplet, we doped the oil phase with Nile Red (Sigma-Aldrich) dye. We performed fluorescent microscopy on an Olympus IX81 microscope with a filter cube (excitation filter ET560/40x, beam splitter 585 LP and emissions filter ET630/75m, all Chroma Technology). Images were captured via a 4x objective using a 4 MP CMOS camera (FLIR Grasshopper 3, GS3-U3-41C6M-C) at 4 fps.

Appendix I: Digital image processing and data analysis

We extracted droplet coordinates from bright field microscopy using a sequence of background correction, binarization, blob detection by contour analysis, and minimum enclosing circle fits, and determined trajectories via a nearest-neighbor algorithm using in-house Python scripts building on numpy and opencv. For the strongly overexposed fluorescence data the droplet centroid was calculated via a distance transform algorithm on the fluorescence intensity. The polar intensity map in Fig. 3(b) was derived by taking the intensity in an annular region around the droplet at a distance of 1.2 droplet radii from the centroid [24, 56, 57], as sketched in supporting figure I.1.

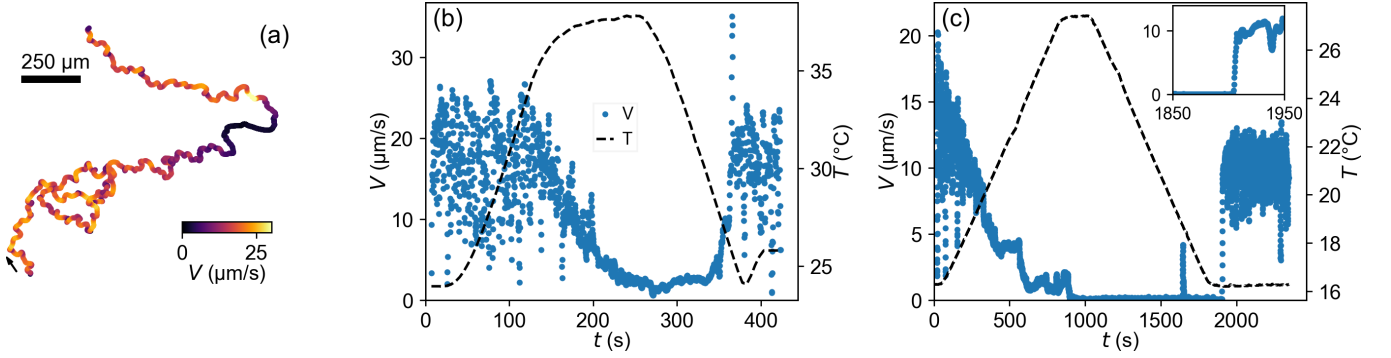


FIG. F.1. Reduced hysteresis during an incomplete heating/cooling cycle. (a) speed coded trajectory (b) Speed and temperature versus time (c) The same quantities for a temperature ramp heating to full droplet arrest, using the data from Fig. 1a.

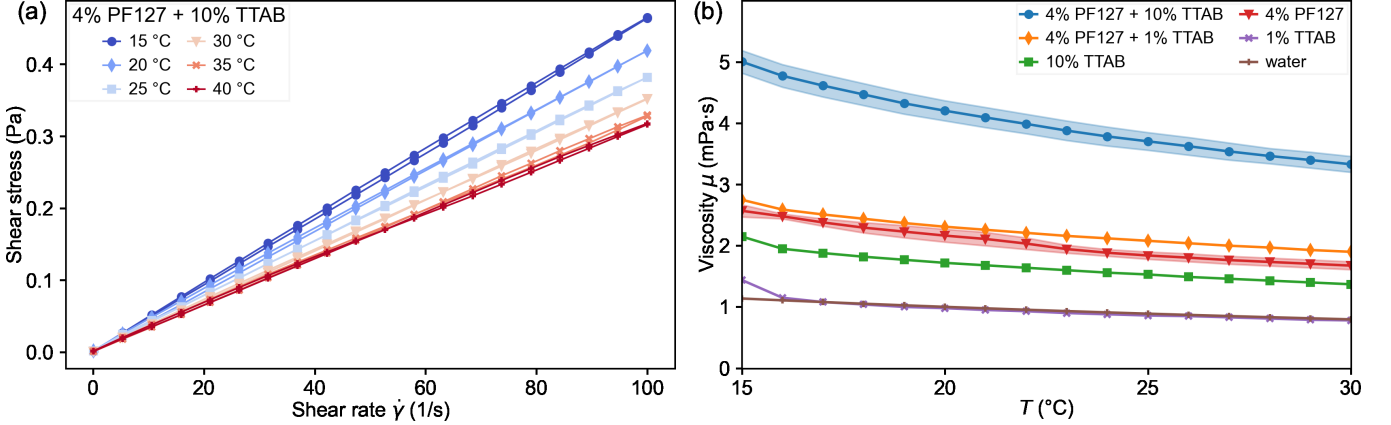


FIG. G.1. (a) Shear stress versus shear rates at different temperatures for 4 wt% PF127 + 10 wt% TTAB. (b) Viscosity versus temperature for TTAB and PF127.

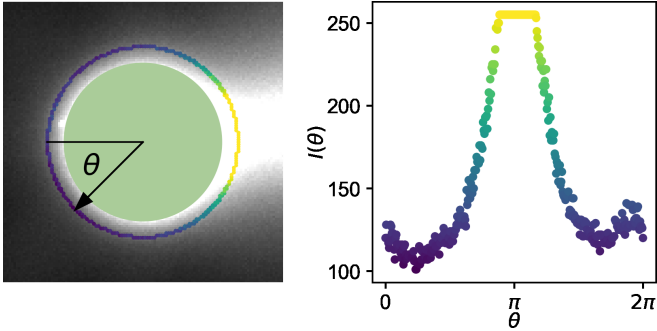


FIG. I.1. Protocol to extract fluorescence kymographs from microvideo data, by the example of snapshot III from Fig. 3

Using the time-dependent droplet trajectory and temperature data, we estimated transition temperatures between dynamic states. The error bars for temperature in the regime map (Fig. 2f) represent the maximum variation within three different runs on samples containing on the order of 5–10 droplets each. It should be noted that there is some uncertainty associated with estimating T_{straight} and T_{stop} from low magnification droplet trajectory data. As seen in high magnification data in Movie

S5, a droplet could appear to be stationary even though it shows internal activity through the motion of tracer particles. Moreover, the transition between a smooth re-orientation and straight motion is somewhat gradual.

We performed PIV analyses using the Matlab PIVlab module [69] with a multi-pass interrogation window of 64×64 pixel and 32×32 pixel with 50% overlap. The spatial resolution of the PIV output was $4.3 \mu\text{m}/\text{px}$.

Appendix J: Numerics

We simulate a diffusiophoretic particle of unit radius initially located at the center of a domain of size $L_x = 10$, $L_y = 100$, $L_z = 2.2$ with $201 \times 2001 \times 45$ grids at sub-critical Pe . The particle is propelled by diffusiophoresis, a type of microswimmer similar to active droplet, as both move in response to the forces at the surfaces, which depend on the local chemical concentration field (see also [52]). The chemical reaction takes place at the particle surface and whenever there is a chemical concentration difference along the surface, a flow is generated within the interaction layer near the solid surface, with thickness λ of nanometers, which propels the particle for-

ward.

We use the same non-dimensional governing equations and boundary conditions at the particle interface as those in previous studies [20, 70] (here, solving for the full 3D problem as opposed to the axisymmetric analytical approach). The governing equations are given as

$$\frac{\partial c}{\partial t} + \mathbf{u} \cdot \nabla c = \frac{1}{Pe} \nabla^2 c, \quad (\text{J1})$$

$$\frac{\partial \mathbf{u}}{\partial t} + (\mathbf{u} \cdot \nabla) \mathbf{u} = -\nabla p + \frac{Sc}{Pe} \nabla^2 \mathbf{u}, \quad \nabla \cdot \mathbf{u} = 0, \quad (\text{J2})$$

where c is the concentration, u the velocity. Pe is the Péclet number, which is the ratio of advection to diffusion and Sc is the Schmidt number, which is the ratio between the momentum and mass diffusivities:

$$Pe = \frac{M\alpha L}{D^2}, \quad Sc = \frac{\nu}{D}. \quad (\text{J3})$$

where M is the mobility, $M \sim \pm k_B T \lambda^2 / (\rho \nu)$ with k_B the Boltzmann constant and T the temperature, ρ the density, ν the viscosity, and D is the diffusion coefficient.

The boundary conditions are given as:

$$\partial_n c = -1 \quad u_s = \nabla_s c, \quad (\text{J4})$$

where $\partial_n c$ represents the concentration gradient at the direction normal to particle surface, u_s the slip velocity and ∇_s is the tangential gradient. The top and bottom boundaries (at z direction) of the domain are set as solid walls, and all other domain boundaries (at x and y directions) are set as periodic.

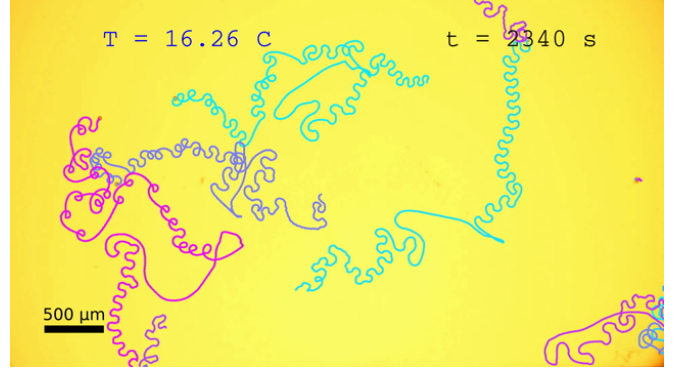
We used a central second-order finite difference scheme to spatially discretize the governing equations, with homogeneous staggered grids used in both the horizontal and vertical directions. The equations are integrated by a fractional-step method, with non-linear terms computed explicitly using a low-storage third-order Runge-Kutta scheme and the viscous terms computed implicitly by a Crank-Nicolson scheme [71]. For the particle boundary, we make use of the moving least squares (MLS) based immersed boundary (IB) method, where the particle interface is represented by a triangulated Lagrangian mesh [72]. For the detailed numerical methods and validation, we refer to [70].

In simulations, we observed the onset of symmetry breaking for $Pe \gtrsim 6$; the velocity profile in the inset of Fig. 4a is taken from a simulation with $Pe = 8$. In Fig. 4(a), the numerical timescale has been re-dimensionalised using the characteristic time and velocity scales t^* and V^* following [20, 58]

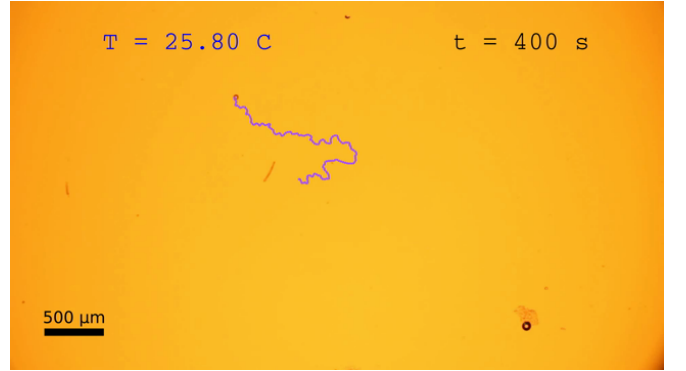
$$Pe = \frac{R \cdot V^*}{D} \quad t^* = \frac{R}{V^*} = \frac{R^2}{Pe \cdot D}$$

with $D \approx 5 \times 10^{-10} \text{ m}^2/\text{s}$ for the Stokes-Einstein diffusivity of a surfactant monomer [24], $R = 25 \mu\text{m}$ and $Pe = 8$.

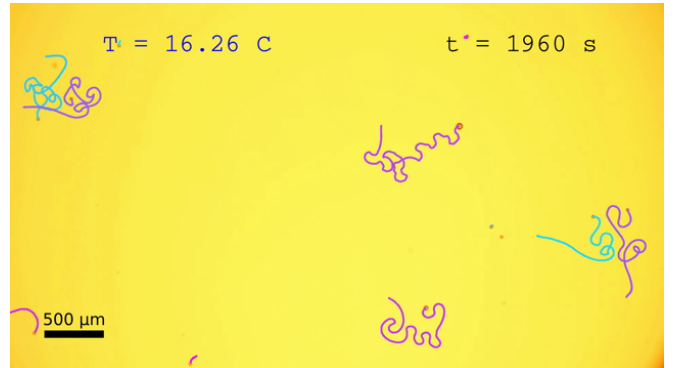
Appendix K: Supplementary Movie captions



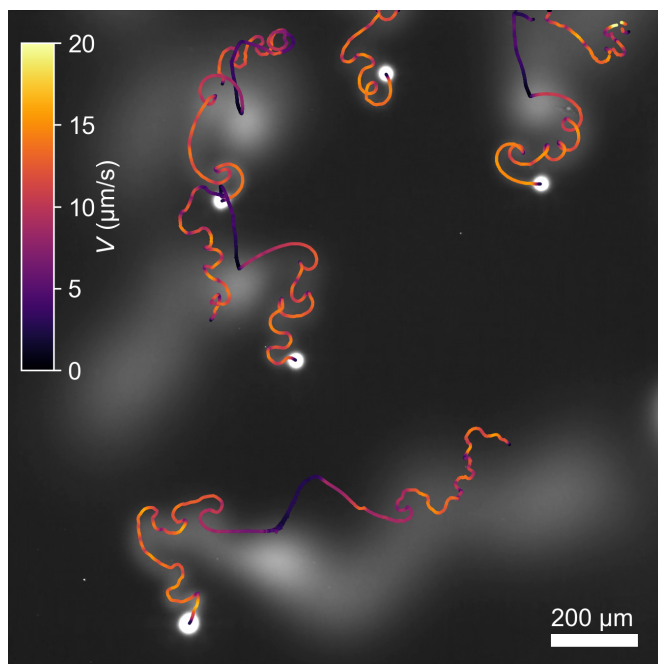
Movie S1. Temperature dependent droplet dynamics at 4 wt% PF127 + 10 wt% TTAB, showing a reversible transition from meandering to straight swimming to arrest during a heating and subsequent cooling ramp with a set rate of 1 K/min.



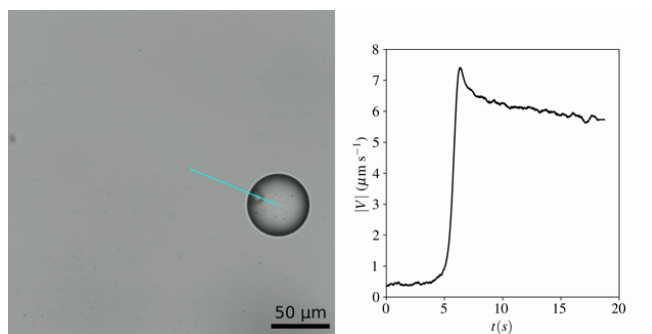
Movie S2. Temperature dependent droplet dynamics at 4 wt% PF127 + 13 wt% TTAB, showing a reversible transition from unsteady to straight swimming to arrest during a heating and subsequent cooling ramp with a set rate of 5 K/min



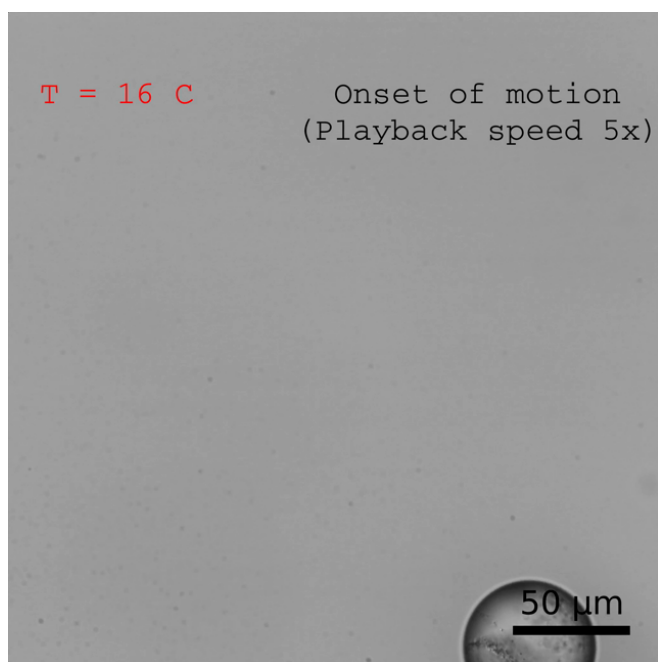
Movie S3. Droplet trajectory at 4 wt% PF127 + 10 wt% TTAB, during multiple heating and subsequent cooling ramps at a set rate of 10 K/min.



Movie S4. Fluorescent microscopy visualising droplet chemical trails upon heating and subsequent cooling ramp with a set rate of 5 K/min.



Movie S6. Onset of active motion during recoiling in a droplet containing tracer colloids, with a superimposed trajectory and the recorded droplet speed V . Experimental duration 18 seconds.



Movie S5. Internal flow visualisation with increasing temperature, starting at a mixed dipolar/quadrupolar mode (meandering), over a purely dipolar mode (straight) that recedes to the anterior (slowdown) and onset of motion during cooling. Excerpts recorded during one continuous experiment, playback (at 40 fps) corresponding to real-time during heating, sped up by 5x during cooling.

- [1] M. J. Bowick, N. Fakhri, M. C. Marchetti, and S. Ramaswamy, "Symmetry, Thermodynamics, and Topology in Active Matter," *Phys. Rev. X* **12**, 010501 (2022).
- [2] J. W. von Goethe, "Der Zauberlehrling," in *Musen-Almanach Für Das Jahr 1798*, edited by F. Schiller (J.G. Cotta, 1798) pp. 32–37.
- [3] J. O'Byrne, Y. Kafri, J. Tailleur, and F. van Wijland, "Time irreversibility in active matter, from micro to macro," *Nat Rev Phys* **4**, 167–183 (2022).
- [4] Y. Tu, F. Peng, and D. A. Wilson, "Motion Manipulation of Micro- and Nanomotors," *Advanced Materials* **29**, 1701970 (2017).
- [5] A. D. Fusi, Y. Li, A. Llopis-Lorente, T. Patiño, J. C. M. van Hest, and L. K. E. A. Abdelmohsen, "Achieving Control in Micro-/Nanomotor Mobility," *Angewandte Chemie International Edition* **62**, e202214754 (2023).
- [6] C. Bechinger, R. Di Leonardo, H. Löwen, C. Reichhardt, G. Volpe, and G. Volpe, "Active Particles in Complex and Crowded Environments," *Reviews of Modern Physics* **88**, 045006 (2016).
- [7] J. Moran and J. Posner, "Microswimmers with no moving parts," *Physics Today* **72**, 44–50 (2019).
- [8] Y. Zhang and H. Hess, "Chemically-powered swimming and diffusion in the microscopic world," *Nat Rev Chem* **5**, 500–510 (2021).
- [9] A. Zöttl and H. Stark, "Modeling Active Colloids: From Active Brownian Particles to Hydrodynamic and Chemical Fields," *Annual Review of Condensed Matter Physics* **14**, 109–127 (2023).
- [10] C. C. Maass, C. Krüger, S. Herminghaus, and C. Bahr, "Swimming Droplets," *Annu. Rev. Condens. Matter Phys.* **7**, 171–193 (2016).
- [11] D. Babu, N. Katsonis, F. Lancia, R. Plamont, and A. Ryabchun, "Motile behaviour of droplets in lipid systems," *Nat Rev Chem* **6**, 377–388 (2022).
- [12] S. Birrer, S. I. Cheon, and L. D. Zarzar, "We the droplets: A constitutional approach to active and self-propelled emulsions," *Current Opinion in Colloid & Interface Science* **61**, 101623 (2022).
- [13] P. Dwivedi, D. Pillai, and R. Mangal, "Self-propelled swimming droplets," *Current Opinion in Colloid & Interface Science* **61**, 101614 (2022).
- [14] S. Michelin, "Self-Propulsion of Chemically Active Droplets," *Annual Review of Fluid Mechanics* **55**, 77–101 (2023).
- [15] M. M. Hanczyc, T. Toyota, T. Ikegami, N. Packard, and T. Sugawara, "Fatty Acid Chemistry at the Oil-Water Interface: Self-Propelled Oil Droplets," *J. Am. Chem. Soc.* **129**, 9386–9391 (2007).
- [16] S. Thutupalli, R. Seemann, and S. Herminghaus, "Swarming behavior of simple model squirmers," *New J. Phys.* **13**, 073021 (2011).
- [17] K. Peddireddy, P. Kumar, S. Thutupalli, S. Herminghaus, and C. Bahr, "Solubilization of thermotropic liquid crystal compounds in aqueous surfactant solutions." *Langmuir* **28**, 12426–31 (2012).
- [18] Z. Izri, M. N. van der Linden, S. Michelin, and O. Dautot, "Self-Propulsion of Pure Water Droplets by Spontaneous Marangoni-Stress-Driven Motion," *Phys. Rev. Lett.* **113**, 248302 (2014).
- [19] S. Herminghaus, C. C. Maass, C. Krüger, S. Thutupalli, L. Goehring, and C. Bahr, "Interfacial mechanisms in active emulsions," *Soft Matter* **10**, 7008–7022 (2014).
- [20] S. Michelin, E. Lauga, and D. Bartolo, "Spontaneous autophoretic motion of isotropic particles," *Physics of Fluids* **25**, 061701 (2013).
- [21] M. Suga, S. Suda, M. Ichikawa, and Y. Kimura, "Self-propelled motion switching in nematic liquid crystal droplets in aqueous surfactant solutions," *Phys. Rev. E* **97**, 062703 (2018).
- [22] A. Izzet, P. G. Moerman, P. Gross, J. Groenewold, A. D. Hollingsworth, J. Bibette, and J. Brujic, "Tunable Persistent Random Walk in Swimming Droplets," *Phys. Rev. X* **10**, 021035 (2020).
- [23] C. H. Meredith, P. G. Moerman, J. Groenewold, Y.-J. Chiu, W. K. Kegel, A. van Blaaderen, and L. D. Zarzar, "Predator-prey interactions between droplets driven by non-reciprocal oil exchange," *Nature Chemistry* **12**, 1136–1142 (2020).
- [24] B. V. Hokmabad, R. Dey, M. Jalaal, D. Mohanty, M. Almukambetova, K. A. Baldwin, D. Lohse, and C. C. Maass, "Emergence of Bimodal Motility in Active Droplets," *Phys. Rev. X* **11**, 011043 (2021).
- [25] S. Suda, T. Suda, T. Ohmura, and M. Ichikawa, "Straight-to-Curvilinear Motion Transition of a Swimming Droplet Caused by the Susceptibility to Fluctuations," *Phys. Rev. Lett.* **127**, 088005 (2021).
- [26] Y. Tu, F. Peng, X. Sui, Y. Men, P. B. White, J. C. M. van Hest, and D. A. Wilson, "Self-propelled supramolecular nanomotors with temperature-responsive speed regulation," *Nature Chemistry* **9**, 480–486 (2017).
- [27] D. Cholokova, M. Lisicki, S. K. Smoukov, S. Tcholakova, E. E. Lin, J. Chen, G. De Canio, E. Lauga, and N. Denkov, "Rechargeable self-assembled droplet microswimmers driven by surface phase transitions," *Nature Physics* **17**, 1050–1055 (2021).
- [28] L. Florea, K. Wagner, P. Wagner, G. G. Wallace, F. Benito-Lopez, D. L. Officer, and D. Diamond, "Photo-Chemopropulsion – Light-Stimulated Movement of Microdroplets," *Advanced Materials* **26**, 7339–7345 (2014).
- [29] S. Kaneko, K. Asakura, and T. Banno, "Phototactic behavior of self-propelled micrometer-sized oil droplets in a surfactant solution," *Chem. Commun.* **53**, 2237–2240 (2017).
- [30] Y. Xiao, S. Zarghami, K. Wagner, P. Wagner, K. C. Gordon, L. Florea, D. Diamond, and D. L. Officer, "Moving Droplets in 3D Using Light," *Advanced Materials* **30**, 1801821 (2018).
- [31] F. Lancia, T. Yamamoto, A. Ryabchun, T. Yamaguchi, M. Sano, and N. Katsonis, "Reorientation behavior in the helical motility of light-responsive spiral droplets," *Nature Communications* **10**, 5238 (2019).
- [32] L. Alvarez, M. A. Fernandez-Rodriguez, A. Alegria, S. Arrese-Igor, K. Zhao, M. Kröger, and L. Isa, "Reconfigurable artificial microswimmers with internal feedback," *Nature Communications* **12**, 4762 (2021).
- [33] A. Ryabchun, D. Babu, J. Movilli, R. Plamont, M. C. A. Stuart, and N. Katsonis, "Run-and-halt motility of droplets in response to light," *Chem* **8**, 2290–2300 (2022).
- [34] M. Y. Ben Zion, Y. Caba, A. Modin, and P. M. Chaikin, "Cooperation in a fluid swarm of fuel-free microswimmers," *Nat Commun* **13**, 184 (2022).

- [35] S. van Kesteren, L. Alvarez, S. Arrese-Igor, A. Alegria, and L. Isa, "Self-propelling colloids with finite state dynamics," *Proceedings of the National Academy of Sciences* **120**, e2213481120 (2023).
- [36] K. C. Tam and E. Wyn-Jones, "Insights on polymer surfactant complex structures during the binding of surfactants to polymers as measured by equilibrium and structural techniques," *Chemical Society Reviews* **35**, 693–709 (2006).
- [37] R. Zhang, A. Mozaffari, and J. J. de Pablo, "Autonomous materials systems from active liquid crystals," *Nature Reviews Materials*, 1–17 (2021).
- [38] J. S. Nambam and J. Philip, "Effects of Interaction of Ionic and Nonionic Surfactants on Self-Assembly of PEO–PPO–PEO Triblock Copolymer in Aqueous Solution," *The Journal of Physical Chemistry B* **116**, 1499–1507 (2012).
- [39] C. Jin, C. Krüger, and C. C. Maass, "Chemotaxis and autochemotaxis of self-propelling droplet swimmers," *PNAS* **114**, 5089–5094 (2017).
- [40] M. J. Rosen and J. T. Kunjappu, *Surfactants and Interfacial Phenomena*, 4th ed. (Wiley, Hoboken, N.J., 2012).
- [41] B. V. Hokmabad, A. Nishide, P. Ramesh, C. Krüger, and C. C. Maass, "Spontaneously rotating clusters of active droplets," *Soft Matter* **18**, 2731–2741 (2022).
- [42] P. Alexandridis, J. F. Holzwarth, and T. A. Hatton, "Micellization of Poly(ethylene oxide)-Poly(propylene oxide)-Poly(ethylene oxide) Triblock Copolymers in Aqueous Solutions: Thermodynamics of Copolymer Association," *Macromolecules* **27**, 2414–2425 (1994).
- [43] G. Wanka, H. Hoffmann, and W. Ulbricht, "Phase Diagrams and Aggregation Behavior of Poly(oxyethylene)-Poly(oxypropylene)-Poly(oxyethylene) Triblock Copolymers in Aqueous Solutions," *Macromolecules* **27**, 4145–4159 (1994).
- [44] M. Bohorquez, C. Koch, T. Trygstad, and N. Pandit, "A Study of the Temperature-Dependent Micellization of Pluronic F127," *Journal of Colloid and Interface Science* **216**, 34–40 (1999).
- [45] B. Stoeber, C.-M. J. Hu, D. Liepmann, and S. J. Muller, "Passive flow control in microdevices using thermally responsive polymer solutions," *Physics of Fluids* **18**, 053103 (2006).
- [46] M. Jalaal, G. Cottrell, N. Balmforth, and B. Stoeber, "On the rheology of Pluronic F127 aqueous solutions," *Journal of Rheology* **61**, 139–146 (2016).
- [47] M. Jalaal, C. Seyfert, B. Stoeber, and N. J. Balmforth, "Gel-controlled droplet spreading," *Journal of Fluid Mechanics* **837**, 115–128 (2018).
- [48] E. Hecht and H. Hoffmann, "Interaction of ABA block copolymers with ionic surfactants in aqueous solution," *Langmuir* **10**, 86–91 (1994).
- [49] Y. Li, R. Xu, S. Couderc, D. M. Bloor, J. F. Holzwarth, and E. Wyn-Jones, "Binding of Tetradecyltrimethylammonium Bromide to the ABA Block Copolymer Pluronic F127 (EO97 PO69 EO97): Electromotive Force, Microcalorimetry, and Light Scattering Studies," *Langmuir* **17**, 5742–5747 (2001).
- [50] H.-J. Butt, K. Graf, and M. Kappl, *Physics and Chemistry of Interfaces* (John Wiley & Sons, 2003).
- [51] E. Hecht, K. Mortensen, M. Gradzielski, and H. Hoffmann, "Interaction of ABA Block Copolymers with Ionic Surfactants: Influence on Micellization and Gelation," *J. Phys. Chem.* **99**, 4866–4874 (1995).
- [52] M. Morozov and S. Michelin, "Nonlinear dynamics of a chemically-active drop: From steady to chaotic self-propulsion," *J. Chem. Phys.* **150**, 044110 (2019).
- [53] M. Morozov, "Adsorption inhibition by swollen micelles may cause multistability in active droplets," *Soft Matter* **16**, 5624–5632 (2020).
- [54] G. Li, "Swimming dynamics of a self-propelled droplet," *Journal of Fluid Mechanics* **934** (2022), 10.1017/jfm.2021.1154.
- [55] W.-F. Hu, T.-S. Lin, S. Rafai, and C. Misbah, "Spontaneous locomotion of phoretic particles in three dimensions," *Phys. Rev. Fluids* **7**, 034003 (2022).
- [56] P. Ramesh, B. V. Hokmabad, D. O. Pushkin, A. J. T. M. Mathijssen, and C. C. Maass, "Interfacial activity dynamics of confined active droplets," *Journal of Fluid Mechanics* **966**, A29 (2023).
- [57] B. V. Hokmabad, J. Agudo-Canalejo, S. Saha, R. Golestanian, and C. C. Maass, "Chemotactic self-caging in active emulsions," *Proceedings of the National Academy of Sciences* **119**, e2122269119 (2022).
- [58] F. Picella and S. Michelin, "Confined self-propulsion of an isotropic active colloid," *Journal of Fluid Mechanics* **933** (2022), 10.1017/jfm.2021.1081.
- [59] M. Schmitt and H. Stark, "Swimming active droplet: A theoretical analysis," *EPL* **101**, 44008 (2013).
- [60] G. G. Peng and O. Schmitzer, "Weakly nonlinear dynamics of a chemically active particle near the threshold for spontaneous motion. II. History-dependent motion," *Phys. Rev. Fluids* **8**, 033602 (2023).
- [61] J. L. Anderson, "Colloid transport by interfacial forces," *Annual Review of Fluid Mechanics* **21**, 61–99 (1989).
- [62] D. Babu, R. J. H. Scanes, R. Plamont, A. Ryabchun, F. Lancia, T. Kudernac, S. P. Fletcher, and N. Katsomis, "Acceleration of lipid reproduction by emergence of microscopic motion," *Nat Commun* **12**, 2959 (2021).
- [63] C. M. Wentworth, A. C. Castonguay, P. G. Moerman, C. H. Meredith, R. V. Balaj, S. I. Cheon, and L. D. Zarzar, "Chemically Tuning Attractive and Repulsive Interactions between Solubilizing Oil Droplets," *Angewandte Chemie International Edition* **61**, e202204510 (2022).
- [64] A. Parmar, S. Chavda, and P. Bahadur, "Pluronic-cationic surfactant mixed micelles: Solubilization and release of the drug hydrochlorothiazide," *Colloids and Surfaces A: Physicochemical and Engineering Aspects* **441**, 389–397 (2014).
- [65] S. Thutupalli, D. Geyer, R. Singh, R. Adhikari, and H. A. Stone, "Flow-induced phase separation of active particles is controlled by boundary conditions," *PNAS* **115**, 5403–5408 (2018).
- [66] T. Lopez-Leon and A. Fernandez-Nieves, "Drops and shells of liquid crystal," *Colloid Polym. Sci.* **289**, 345–359 (2011).
- [67] J. Shechter, N. Atzin, A. Mozaffari, R. Zhang, Y. Zhou, B. Strain, L. M. Oster, J. J. de Pablo, and J. L. Ross, "Direct Observation of Liquid Crystal Droplet Configurational Transitions using Optical Tweezers," *Langmuir* **36**, 7074–7082 (2020).
- [68] A. J. Kim, V. N. Manoharan, and J. C. Crocker, "Swelling-Based Method for Preparing Stable, Functionalized Polymer Colloids," *J. Am. Chem. Soc.* **127**, 1592–1593 (2005).
- [69] W. Thielicke and E. Stamhuis, "PIVlab – Towards User-friendly, Affordable and Accurate Digital Particle Image

- Velocimetry in MATLAB,” *JORS* **2**, e30 (2014).
- [70] Y. Chen, K. L. Chong, L. Liu, R. Verzicco, and D. Lohse, “Instabilities driven by diffusiophoretic flow on catalytic surfaces,” *Journal of Fluid Mechanics* **919**, A10 (2021).
- [71] R. Verzicco and P. Orlandi, “A Finite-Difference Scheme for Three-Dimensional Incompressible Flows in Cylindrical Coordinates,” *Journal of Computational Physics* **123**, 402–414 (1996).
- [72] V. Spandan, V. Meschini, R. Ostilla-Mónico, D. Lohse, G. Querzoli, M. D. de Tullio, and R. Verzicco, “A parallel interaction potential approach coupled with the immersed boundary method for fully resolved simulations of deformable interfaces and membranes,” *Journal of Computational Physics* **348**, 567–590 (2017).